

Controllable optomechanical coupling and Drude self-pulsation plasma locking in chip-scale optomechanical cavities

YONGJUN HUANG,^{1,2,*} JAIME GONZALO FLOR FLORES,² ZIQIANG CAI,²
JIAGUI WU,^{2,3} MINGBIN YU,⁴ DIM-LEE KWONG,⁴ GUANGJUN WEN,¹ LAYNE
CHURCHILL,⁵ AND CHEE WEI WONG²

¹*School of Communication and Information Engineering, University of Electronic Science and Technology of China, Chengdu, 611731, China*

²*Fang Lu Mesoscopic Optics and Quantum Electronics Laboratory, University of California, Los Angeles, CA 90095, USA*

³*College of Electronic and Information Engineering, Southwest University, Chongqing 400715, China*

⁴*Institute of Microelectronics, A*STAR 117865, Singapore*

⁵*Georgia Tech. Research Institute, Atlanta, GA 30318, USA*

*yongjunh@uestc.edu.cn

Abstract: We demonstrate the controllable optomechanical coupling and Drude self-pulsation plasma locking in chip-scale optomechanical cavities. The optomechanical coupling between the optical and mechanical degrees-of-freedom is dependent on the intracavity energy via the coupled fiber position. With the deterministic optomechanical stiffening, the interaction between optomechanical oscillation and self-pulsation can be controlled. Intracavity locking with 1/6 subharmonics is obtained over a wide optical detuning range of 190.01–192.23 THz. These results bring new insights into implementations of nonlinear dynamics at mesoscopic scale, with potential applications from photonic signal processing to nonlinear dynamic networks.

© 2017 Optical Society of America

OCIS codes: (230.5298) Photonic crystals; (230.5750) Resonators; (220.4880) Optomechanics; (230.4685) Optical microelectromechanical devices.

References and links

1. M. Aspelmeyer, T. J. Kippenberg, and F. Marquardt, "Cavity optomechanics," *Rev. Mod. Phys.* **86**(4), 1391–1452 (2014).
2. J. D. Teufel, T. Donner, D. Li, J. W. Harlow, M. S. Allman, K. Cicak, A. J. Sirois, J. D. Whittaker, K. W. Lehnert, and R. W. Simmonds, "Sideband cooling of micromechanical motion to the quantum ground state," *Nature* **475**(7356), 359–363 (2011).
3. Y.-C. Liu, Y. F. Xiao, X. Luan, and C. W. Wong, "Dynamic dissipative cooling of a mechanical resonator in strong coupling optomechanics," *Phys. Rev. Lett.* **110**(15), 153606 (2013).
4. Y.-C. Liu, Y.-F. Xiao, X. Luan, Q. Gong, and C. W. Wong, "Coupled cavities for motional ground-state cooling and strong optomechanical coupling," *Phys. Rev. A* **91**(3), 033818 (2015).
5. A. H. Safavi-Naeini, T. P. M. Alegre, J. Chan, M. Eichenfield, M. Winger, Q. Lin, J. T. Hill, D. E. Chang, and O. Painter, "Electromagnetically induced transparency and slow light with optomechanics," *Nature* **472**(7341), 69–73 (2011).
6. M. Hossein-Zadeh and K. J. Vahala, "An optomechanical oscillator on a silicon chip," *IEEE J. Sel. Top. Quantum Electron.* **16**(1), 276–287 (2010).
7. H. Miao, K. Srinivasan, and V. Aksyuk, "A microelectromechanically controlled cavity optomechanical sensing system," *New J. Phys.* **14**(7), 075015 (2012).
8. E. Gavartin, P. Verlot, and T. J. Kippenberg, "A hybrid on-chip optomechanical transducer for ultrasensitive force measurements," *Nat. Nanotechnol.* **7**(8), 509–514 (2012).
9. A. G. Krause, M. Winger, T. D. Blasius, Q. Lin, and O. Painter, "A high-resolution microchip optomechanical accelerometer," *Nat. Photonics* **6**(11), 768–772 (2012).
10. F. Guzmán Cervantes, L. Kumanchik, J. Pratt, and J. M. Taylor, "High sensitivity optomechanical reference accelerometer over 10 kHz," *Appl. Phys. Lett.* **104**(22), 221111 (2014).
11. C. Comi, A. Corigliano, G. Langfelder, A. Longoni, A. Tocchio, and B. Simoni, "A resonant microaccelerometer with high sensitivity operating in an oscillating circuit," *J. Micromech. Syst.* **19**(5), 1140–1152 (2010).

12. J. G. F. Flores, Y. Huang, Y. Li, Z. Cai, V. Iaia, M. Yu, D.-L. Kwong, L. Churchill, and C. W. Wong, "A chip-scale sub-mg/Hz^{1/2} optomechanical DC accelerometer at the thermodynamical limit," in *Proceedings of CLEO: Applications and Technology*, (Optical Society of America, 2016), paper AM4K. 6.
13. Y. Li, J. Zheng, J. Gao, J. Shu, M. S. Aras, and C. W. Wong, "Design of dispersive optomechanical coupling and cooling in ultrahigh- Q/V slot-type photonic crystal cavities," *Opt. Express* **18**(23), 23844–23856 (2010).
14. J. Zheng, X. Sun, Y. Li, M. Poot, A. Dadgar, N. N. Shi, W. H. P. Pernice, H. X. Tang, and C. W. Wong, "Femtogram dispersive L3-nanobeam optomechanical cavities: design and experimental comparison," *Opt. Express* **20**(24), 26486–26498 (2012).
15. X. Luan, Y. Huang, Y. Li, J. F. McMillan, J. Zheng, S.-W. Huang, P.-C. Hsieh, T. Gu, D. Wang, A. Hati, D. A. Howe, G. Wen, M. Yu, G. Lo, D.-L. Kwong, and C. W. Wong, "An integrated low phase noise radiation-pressure-driven optomechanical oscillator chipset," *Sci. Rep.* **4**, 6842 (2014).
16. J. Gao, J. F. McMillan, M.-C. Wu, J. Zheng, S. Assefa, and C. W. Wong, "Demonstration of an air-slot mode-gap confined photonic crystal slab nanocavity with ultrasmall mode volumes," *Appl. Phys. Lett.* **96**(5), 051123 (2010).
17. J. Yang, T. Gu, J. Zheng, M. Yu, G.-Q. Lo, D.-L. Kwong, and C. W. Wong, "Radio frequency regenerative oscillations in monolithic high- Q/V heterostructured photonic crystal cavities," *Appl. Phys. Lett.* **104**(6), 061104 (2014).
18. T. Yamamoto, M. Notomi, H. Taniyama, E. Kuramochi, Y. Yoshikawa, Y. Torii, and T. Kuga, "Design of a high- Q air-slot cavity based on a width-modulated line-defect in a photonic crystal slab," *Opt. Express* **16**(18), 13809–13817 (2008).
19. J. Gao, P. Heider, C. J. Chen, X. Yang, C. A. Husko, and C. W. Wong, "Observations of interior whispering gallery modes in asymmetric optical resonators with rational caustics," *Appl. Phys. Lett.* **91**(18), 181101 (2007).
20. D. Navarro-Urrios, N. E. Capuj, J. Gomis-Bresco, F. Alzina, A. Pitanti, A. Griol, A. Martínez, and C. M. Sotomayor Torres, "A self-stabilized coherent phonon source driven by optical forces," *Sci. Rep.* **5**, 15733 (2015).
21. X. Luan, J. F. McMillan, Y. Huang, T. Gu, M. Yu, D.-L. Kwong, and C. W. Wong, "Subharmonics generation based on synchronization of self-pulsation and optomechanical oscillation in a monolithic silicon cavity," in *Proceedings CLEO: QELS Fundamental Science*, (Optical Society of America, 2014), paper JTh5B. 5.
22. J. Wu, Y. Huang, M. Yu, D.-L. Kwong, and C. W. Wong, "Subharmonics radio-frequency division in chip-scale optomechanical oscillators," in *Proceedings CLEO: Science and Innovations*, (Optical Society of America, 2015), paper STh31. 5.
23. T. J. Kippenberg, H. Rokhsari, T. Carmon, A. Scherer, and K. J. Vahala, "Analysis of radiation-pressure induced mechanical oscillation of an optical microcavity," *Phys. Rev. Lett.* **95**(3), 033901 (2005).
24. M. Brunstein, A. M. Yacomotti, I. Sagnes, F. Raineri, L. Bigot, and A. Levenson, "Excitability and self-pulsing in a photonic crystal nanocavity," *Phys. Rev. A* **85**(3), 031803 (2012).
25. Y. Huang, J. G. Flores, Z. Cai, M. Yu, D.-L. Kwong, G. Wen, and C. W. Wong, "Wide optical force-induced RF dynamic range and 100+high-order stable mechanics in chip-scale optomechanical cavities," in *Proceedings of CLEO: Science and Innovations*, (Optical Society of America, 2016), paper STu4E. 7.
26. L. Zhang, Y. Fei, T. Cao, Y. Cao, Q. Xu, and S. Chen, "Multibistability and self-pulsation in nonlinear high- Q silicon microring resonators considering thermo-optical effect," *Phys. Rev. A* **87**(5), 053805 (2013).
27. N. Cazier, X. Chécoury, L.-D. Haret, and P. Boucaud, "High-frequency self-induced oscillations in a silicon nanocavity," *Opt. Express* **21**(11), 13626–13638 (2013).
28. L. Zhang, Y. Fei, Y. Cao, X. Lei, and S. Chen, "Experimental observations of thermo-optical bistability and self-pulsation in silicon microring resonators," *J. Opt. Soc. Am. B* **31**(2), 201–206 (2014).
29. T. J. Johnson, M. Borselli, and O. Painter, "Self-induced optical modulation of the transmission through a high- Q silicon microdisk resonator," *Opt. Express* **14**(2), 817–831 (2006).
30. M. Hossein-Zadeh and K. J. Vahala, "Observation of injection locking in an optomechanical rf oscillator," *Appl. Phys. Lett.* **93**(19), 191115 (2008).

1. Introduction

Recently chip-scale cavity optomechanics on various semiconductor platforms have been realized experimentally [1–12], and wide fundamental classical and quantum phenomena and applications are reported, including ground state cooling [2–4], electromagnetically induced transparency (EIT) [5], and stable RF references [6]. Most of the devices have as small mass as possible to achieve good performances. On another hand, to develop the optomechanical applications for precision force and field sensing [7–10], the test mass of optomechanical cavity should be as large as possible, similar to the MEMS sensors [11]. With increasing test mass, the fundamental mechanical resonance/oscillation mode is shifted to lower frequency such as in the kHz to MHz ranges. For the air-slot photonic crystal (PhC) optomechanical cavities with large test masses to realize the chip scale accelerometers developed previously [12], the laser driving source is coupled into the cavity by anchoring a dimpled fiber taper to the cavity area. Therefore, the position of dimpled fiber taper to cavity is a key parameter for

determining the coupling of laser power to the cavity, and mostly importantly deciding the optomechanical coupling strength due to the perturbation of air slot.

Our silicon-based optomechanical cavity is also an optical slot cavity with sub-wavelength mode volume [13–16]. The strong optical field confined in the slot cavity also modifies the local free-carrier density and temperature through two-photon absorption (TPA), free-carrier dispersions and thermo-optical effects. With controlled laser-cavity detuning and intracavity energies, the cooperative temporal response between the thermal and free-carrier dispersions in an optical resonator can potentially trigger a self-induced RF modulation of the intracavity field, typically referred to as self-pulsation (SP) [17].

In this paper we demonstrate the controllable optomechanical coupling and Drude self-pulsation plasma locking, their controllable relative strengths and subharmonics generation, in chip-scale low-frequency optomechanical cavities. The controllable optomechanical coupling strength is realized by changing the tapered fiber position anchored on the optomechanical cavity and, as a result, the coupling rate between optical and mechanical degree-of-freedom are altered. Due to the interaction between optomechanical oscillation and self-pulsation, the intracavity locking is obtained with 1/6 subharmonics over a wide optical detuning range of 190.01–192.23 THz.

2. Descriptions for the optomechanical cavities

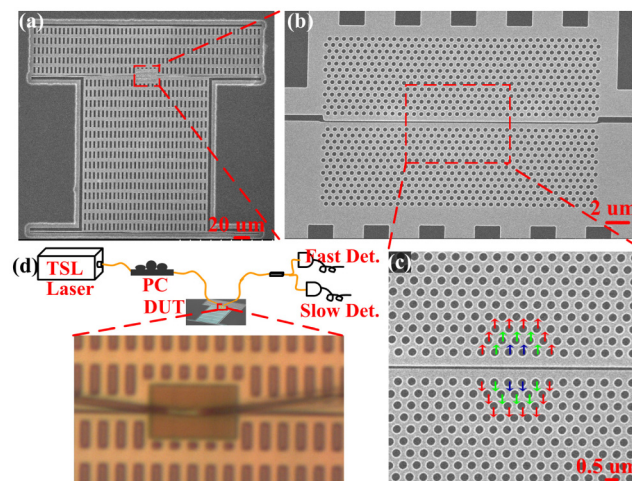


Fig. 1. Scanning electron micrograph (SEM) images for (a) the full size low-frequency optomechanical cavity with large test mass. Scale bar: 20 μm . (b) Zoom-in view showing the air-slot photonic crystal cavity. Scale bar: 2 μm . (c) Zoom-in illustration indicating the lattice perturbations. Scale bar: 500 nm. (d) Tapered fiber measurement setup to characterize the optical and mechanical resonances.

The low-frequency optomechanical cavity is nanofabricated in a silicon-on-insulator substrate with a 250-nm silicon device layer via CMOS-compatible silicon processes (248 nm deep-UV photolithography and reactive ion etching). A scanning electron micrograph (SEM) image of the full-size device is shown in Fig. 1(a). The slot-type PhC cavity is located at the center region [Fig. 1(b)] of the large test mass device. As shown in Fig. 1(c), such cavity fabricated here features a slot width s of 100 nm, PhC lattice constant (a_{pc}) of 470 nm, and hole radii of 150 nm, with 5 nm (red), 10 nm (green) and 15 nm (blue) lattice perturbations (more details can be found in [13,15]). The large 5.6 ng test-mass ($\approx 120 \mu\text{m} \times 150 \mu\text{m}$) has four compliant support beams ($1 \mu\text{m} \times 50 \mu\text{m}$), which can provide a ≈ 78.9 kHz fundamental resonance and a 1.33 N/m combined stiffness. The lower side of the slot-type PhC cavity is attached to large test-mass as illustrated in Fig. 1(a), while the upper side of the cavity is anchored to the substrate. In order to preserve the localized optical resonance mode, the upper side has the

same x -length as the test-mass to reduce asymmetric residual stress z -bow between the two sections. As shown in Fig. 1(a), rectangular holes outside the PhC region are added on both the test-mass (lower side) and the fixed mass (upper side) to shorten the release time in the vapor HF SiO₂ undercut and to improve the release yield.

Figure 1(d) shows the measurement setup in which the optomechanical cavity is probed by a dimpled fiber taper (with more than 90% transmission) under atmospheric pressure, by anchoring the fiber dimple directly on the chip surface and on the lower side [see Fig. 1(a)] of the optomechanical slot cavity. The optical driving source is provided by a tunable laser diode (Santec TSL-510) and a fiber polarization controller is used to select the transverse-electric (TE) state-of-polarization to drive the optomechanical oscillator. Simultaneous readouts of the RF and optical spectra are done with an external fast photodetector (New Focus 125 MHz detector) and slow detector (Thorlabs 125 kHz InGaAs detector), respectively. The measured data are recorded by NI DAQ and LabVIEW programs.

3. Demonstrations of controllable optomechanical coupling

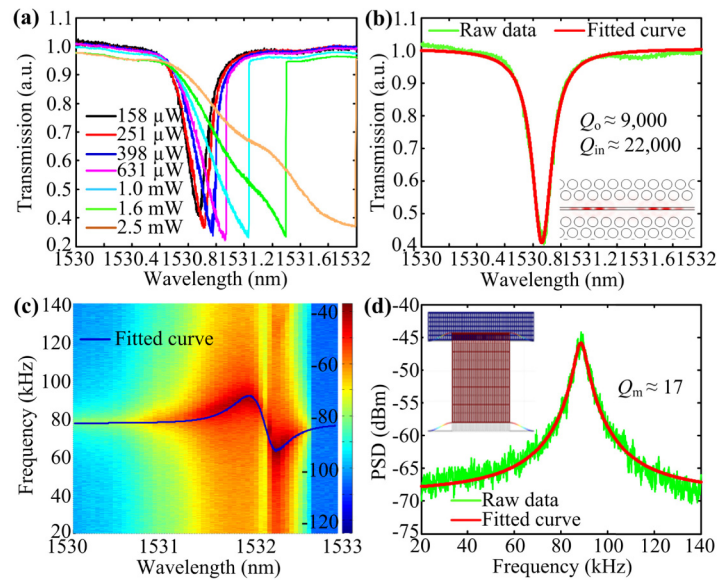


Fig. 2. (a) Optical transmission spectra at different laser drive powers. (b) One example optical transmission spectrum with Lorentzian curve fit at drive power of 158 μ W. (c) Mechanical power spectral densities under different laser detunings. (d) One example mechanical power spectral density with Lorentzian curve fit at blue detuning. The insets of panel (b) and (d) are the corresponding $|E_y|^2$ field distribution of the optical resonance and fundamental mechanical displacement field.

First we demonstrate the optical and mechanical modes by measuring the optical transmission with different drive powers and the mechanical frequency shift with different optical detunings to the optical resonance. As shown in Fig. 2(a), cavity resonance shifts from 1530.87 nm to 1511.49 nm as dropped-in power (estimated power inside the cavity) increases from 158 μ W to 2.5 mW. Through Lorentzian curve-fitting of the cold cavity transmission spectrum (at a dropped-in power of 158 μ W), we obtain the loaded and intrinsic Q factors of 9,000 and 22,000 respectively. The modeled electric field intensity distribution ($|E_y|^2$) of the optical mode is shown in the inset of Fig. 2(b). The Q factors are strongly dependent on the air-slot width of the slot PhC cavity [18], and also related to the edge roughness (estimated to be smaller than 5 nm) of the fabricated pattern [19]. At higher input powers the cavity transmission becomes asymmetric due to thermal nonlinearity and hysteresis, indicated by the sharp transition edges because of the bistable states.

Figure 2(c) shows the measured mechanical power spectral densities, by varying the swept pump wavelength. The mechanical resonance frequency changes with the swept pump wavelength and indicates the canonical optomechanical stiffening which has been analyzed previously [1,13]. In the slot-type optomechanical cavity, the optomechanical stiffening and optical-mechanical resonance spectra of the cavity are strongly dependent on the drive power level and optomechanical coupling rate. Particularly, the resulting modified mechanical frequency resonance can be obtained as:

$$\Omega'_m = \sqrt{\Omega_m^2 + \left(\frac{2|a|^2 g_{om}^2}{((\omega_l - \omega_c)^2 + (\Gamma/2)^2) \omega_c m_x} \right)} (\omega_l - \omega_c). \quad (1)$$

Here Ω'_m (Ω_m) is the shifted (unperturbed) mechanical resonance frequency, $|a|^2$ the averaged intracavity photon energy, ω_c the optical resonance frequency, and $\Gamma = 1/\tau$ the optical cavity decay rate.

The modelled mechanical frequencies for different detunings, corresponding to the dropped-in power in Fig. 2(b), are also superimposed on the measurement as the solid line shown in Fig. 2(c). We estimate the optomechanical coupling rate $g_{om}/2\pi$ to be ≈ 33.5 GHz/nm, with the vacuum optomechanical coupling rate $g^*/2\pi \approx 146$ kHz. We note that the measured g_{om} here is smaller than theoretical prediction [13] due to the difference in height between the motional mass and the fixed beam after release, lowering the optomechanical transduction from designed values. With a blue optical detuning (1531.85 nm), the cold fundamental mechanical mode at atmosphere and room temperature is located at 88.2 kHz. The mechanical modal displacement is shown in the inset of Fig. 2(d).

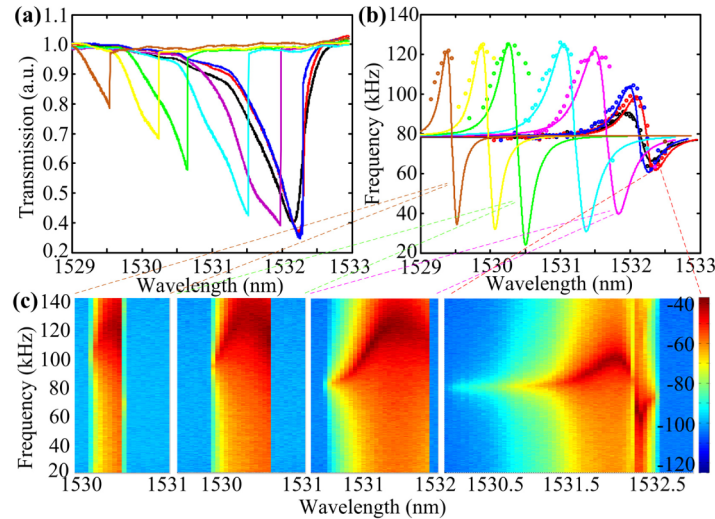


Fig. 3. (a) Optical transmissions at different fiber-cavity coupling positions. (b) Mechanical resonance shifts for laser detunings corresponding to the eight fiber-cavity coupling positions. (c) Two-dimensional mechanical frequency versus laser wavelength maps for four selected coupling positions in panel (b). The eight different colored curves (black, red, blue, purple, cyan, green, yellow, and brown) correspond to the fiber positions continuously changed in one direction.

Next we change the coupled power by altering the fiber position slightly while keeping the input laser power constant at $\sim 158 \mu\text{W}$. As shown in the inset of Fig. 1(d), the dimpled fiber taper is touched physically on one side of the large mass PhC cavity, visualized from the microscope image with piezoelectric actuator control of the fiber position. The different fiber

position controlled by Attocube positioner and scanner changes the height of the large test mass, so alters the optomechanical cavity size shown in Fig. 1(c). As a result, it will change the optical cavity resonance and coupled power, as summarized in Fig. 3(a). This modifies the intracavity photon number. Most importantly, the optomechanical coupling is changed as well. This can be confirmed experimentally in Fig. 3(b), where different optomechanical stiffenings are observed for eight different fiber-cavity couplings.

Considering the first coupling state [black curve in Fig. 3(a)], the mechanical stiffening and softening range is from 65 kHz to 91 kHz [black circle and curve in Fig. 3(b)]. The corresponding fitted optomechanical coupling rate $g_{om}/2\pi$ is ≈ 33.5 GHz/nm. When changing the fiber-cavity laser coupling by piezoelectrically altering the fiber height with respect to the large test mass, the optical transmissions are changed slightly [the red and blue curves in Fig. 3(a)]. The intracavity photon number is increased and the fitted optomechanical coupling rate $g_{om}/2\pi$ is changed to 32.1 GHz/nm and 31.8 GHz/nm correspondingly. With further modification of the fiber-cavity laser coupling (mechanically altering the fiber height in the same direction), the optical resonance with asymmetric lineshape blue shifts strongly, from 1532.27 nm to 1529.53 nm. At the same time, the intracavity photon number is changed accordingly and described by the below equation [9]:

$$n_{cav} = \langle a^\dagger a \rangle = \frac{\kappa_e}{2} \frac{1}{\Delta^2 + \kappa^2 / 4} \frac{P_{in}}{\hbar \omega_l}, \quad (2)$$

where κ_e and κ are the external fiber-cavity coupling rate and the total cavity decay rate, P_{in} the intracavity dropped-in power, $\Delta = \omega_l - \omega_l$ the optical detuning, and \hbar the reduced Planck constant. Figure 3(b) summarized the mechanical resonance shifts for the laser detunings, corresponding to the eight different dimpled fiber taper positions, Fig. 3(c) shows four selected measured raw data for the mechanical power spectral densities for different laser detunings. The corresponding fitted optomechanical coupling rates for each fiber-cavity laser coupling position is illustrated in Table 1.

Table 1. Obtained g_{om} (in GHz/nm) for different fiber-cavity couplings

Positon 1 (black)	Positon 2 (red)	Positon 3 (blue)	Positon 4 (purple)	Positon 5 (cyan)	Positon 6 (green)	Positon 7 (yellow)	Positon 8 (brown)
33.5	32.1	31.8	55.3	60.5	62.6	64.9	73.8

While monotonically changing the fiber-cavity coupling in the same direction piezoelectrically, Table 1 shows that, first, g_{om} is decreased slightly in the initial positions. Then the g_{om} is increased suddenly while modifying the fiber-cavity coupling in the same direction. This interesting phenomenon can be explained as follows. At the beginning coupling positions, the coupling strength is increased gradually as the optical resonance is changed from symmetric Lorentzian to asymmetric lineshapes as shown in Fig. 3(a). This enhances the intracavity energy and the mechanical resonance stiffening range is enlarged accordingly as shown in Fig. 3(b), coinciding with the theoretical relationship as obtained in Eq. (1). In these initial positions, therefore, the g_{om} is not changed strongly.

With continued modification of the fiber-cavity coupling position, the optical resonance blue shifts as shown in Fig. 3(a). At the same time, the fiber-cavity coupling strength is reduced as the transmission dip dropped. Thus the intracavity energy is reduced accordingly. However, as shown in Fig. 3(b), the mechanical resonance stiffening range is enlarged strongly up to 122 kHz. From the fitted curves we get the g_{om} currently larger than 60 GHz/nm. The only feasible explanation is the anchored fiber physically improving the height-to-height planarity of the motional mass and fixed beam (non-planar after release and without the tapered fiber). This pushes the experimental obtained g_{om} is closer to the theoretical modeling. These observations enable the control of the optomechanical coupling by tuning the fiber positions.

4. Demonstrations of Drude self-pulsation plasma locking

Next we demonstrate the Drude self-pulsation plasma locking of the optomechanical cavity, namely the intracavity interaction and locking between optomechanical resonance and self-pulsation oscillation. This has been observed in one-dimensional PhC nanobeam [20] or 100 MHz air-slot PhC optomechanical cavities [21,22] but not yet on the low-frequency (\approx kHz range) for the Drude self-pulsation plasma locking. To excite the self-pulsation oscillation state, the intracavity power should be beyond the threshold of self-pulsation. Furthermore, to excite such self-pulsation oscillation state before the optomechanical self-sustaining oscillation in our air-slot PhC cavity, the threshold of self-pulsation should be below the threshold of optomechanical self-sustaining oscillation. The theoretical scale predictions of such two thresholds are [23,24]:

$$P_{th_OM} \propto \frac{1}{Q_m} \frac{1}{Q_o^3}, \quad (3a)$$

$$P_{th_SP} \propto \frac{V}{Q_o^2}. \quad (3b)$$

Here Q_m and Q_o are the mechanical resonance quality factor and optical resonance quality factor, and V the optical mode volume. For the discussed optomechanical cavity in this paper with such large test-mass and long supporting beams, as shown in Fig. 1(a), the mechanical quality factor is quite low (≈ 17 as shown in previous section) due to the large mechanical loss in room temperature and atmospheric environments. Therefore, the self-pulsation oscillation is always excited before the optomechanical self-sustaining oscillation, along with the small optical mode volume mentioned previously.

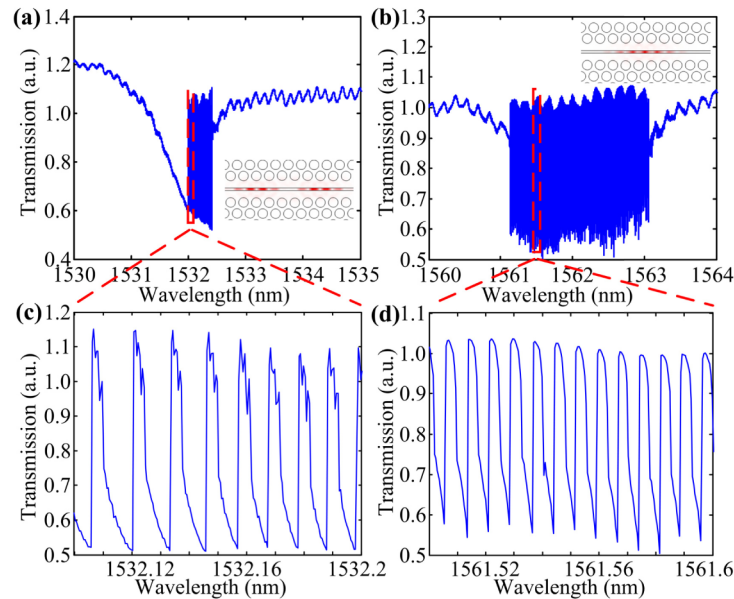


Fig. 4. (a) and (b) Optical transmissions for the two modes under drive power of ≈ 6 mW. (c) and (d) Zoom-in plots which indicate the signatures of exciting self-pulsation oscillation. The insets shown in panel (a) and (b) are the $|E_y|^2$ field distributions of such two optical resonance modes.

As an example, when the drive power reaches to ≈ 6 mW, above the threshold of self-pulsation, the signatures of excited self-pulsation oscillation appear in the optical transmission

as shown in Fig. 4 for two optical modes [25]. The corresponding $|E_y|^2$ field distributions for such two modes are shown in the inset of Figs. 4(a) and 4(b). As shown in the zoom-in plots in Figs. 4(c) and 4(d), the modulated transmission magnitudes of the laser power indicate the signature characteristics of Drude self-pulsation [17, 26–28].

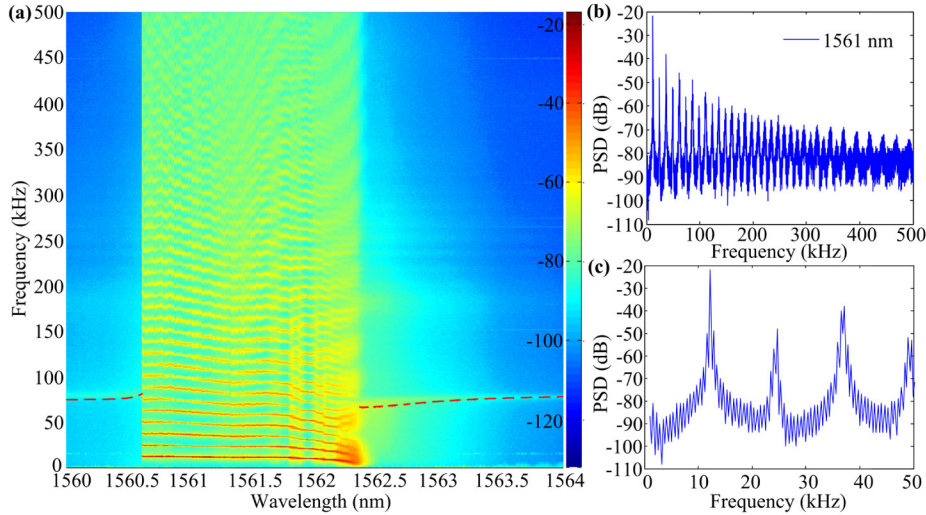


Fig. 5. (a) Two-dimensional map of mechanical frequency power spectral densities versus laser wavelength showing the Drude self-pulsation plasma locking, subharmonics and harmonics. (b) Example power spectral density at laser detuning of 1561 nm and the corresponding zoom-in plot in the frequency range up to 50 kHz.

Likewise as earlier, we collect the readout power spectral densities at different laser detunings and the two-dimensional plot for the fundamental mode is shown in Fig. 5(a). It shows the interesting Drude self-pulsation plasma locking between mechanical resonance and self-pulsation oscillation. Specifically, outside the ≈ 1560.65 nm to 1562.40 nm wavelength regime, there is only the one mechanical resonance which has the similar optomechanical stiffening characteristics as shown in Fig. 2(c). When the pump laser wavelengths are within the range of 1560.65 nm to 1562.40 nm, self-pulsation oscillation are excited and significant subharmonics of the self-pulsation oscillation appear as shown in Fig. 5(a). One example power spectral density at a laser wavelength of 1561 nm is shown in Fig. 5(b) and the corresponding zoom-in plot in the frequency range up to 50 kHz is shown in Fig. 5(c). The frequency of fundamental self-pulsation oscillation can be described by [27]:

$$\Omega \approx \sqrt[5]{\frac{\tau_{fc} \gamma^{TPA} \gamma_i^{FCA}}{2(\hbar\omega)^2 V} \times T_{\max} \left(\frac{P_{in}}{2\tau}\right)^2 - \frac{\Delta\omega}{5}}. \quad (4)$$

Here the defined parameters can be found in [27] as well. As can be seen from Eq. (4), the frequency of self-pulsation is determined by the cavity decay rate (τ), two photon absorption (γ^{TPA}), free-carrier absorption (γ^{FCA}) effects, and the laser detuning ($\Delta\omega$), and with a wide frequency tuning range from kHz to MHz [17,29]. Due to the nonlinear effects, e.g., thermo-optic and free-carriers dispersion, the self-pulsation oscillation has strong harmonics as experimentally and theoretically demonstrated in [17]. As a result, once the harmonics of self-pulsation close to the mechanical resonance at a specific laser detuning, the Drude self-pulsation plasma locking are obtained. This is a classic injection locking process as analyzed by Hossein-Zadeh, et al. [30]. For the examined results as shown in Fig. 5, the sixth order of the fundamental self-pulsation oscillation equals to the fundamental mechanical frequency and we considered it as 1/6 subharmonics. Moreover, harmonics of the lowest frequencies

naturally arises due to the locking of the self-pulsation frequency with optomechanical oscillation. The enhancement of high-order harmonics range is a direct result of the nonlinear transduction of optical field due to self-pulsation, as shown in Fig. 2(a).

5. Summary

Here we have experimentally demonstrated two concurrent interesting characteristics in chip-scale low-frequency optomechanical cavities. The controllable optomechanical coupling is first obtained and demonstrated by controlling the fiber-cavity coupling to the motional silicon photonic crystal membrane. Second, Drude self-pulsation plasma locking with the optomechanical oscillation shows subharmonics, obtained in higher drive laser powers. These results bring new insights into the implementations of nonlinear dynamics in mesoscopic scale, with applications in frequency oscillators and photonic signal processing.

Funding

National Natural Science Foundation of China (NSFC) (61371047, 11474233).

Acknowledgments

The authors thank for the partly supports from the Office of Naval Research, DARPA. The authors also acknowledge discussions with Shu-Wei Huang, Ying Li, and Jinkang Lim.